Perovskite-Type LaCoO 3 as an Efficient and Green Catalyst for Sustainable Partial Oxidation of Cyclohexane

Edgar Muhumuza, Pingping Wu, Tian Nan, Lianming Zhao, Peng Bai, Svetlana Mintova, Zifeng Yan

Perovskite-type $LaCoO_3$ as an Efficient and Green Catalyst for Sustainable Partial Oxidation of Cyclohexane

Edgar Muhumuza,[1,‡] Pingping Wu,[1,‡] Tian Nan,[1] Lianming Zhao,[2] Peng Bai,[1,] Svetlana Mintova,[1,3] and Zifeng Yan[1]*

[1]State Key Laboratory of Heavy Oil Processing, CNPC Key Laboratory of Catalysis, College of Chemical Engineering, China University of Petroleum (East China), Qingdao 266580, China

[2]School of Materials Science and Engineering, Institute of Advanced Materials, China University of Petroleum (East China), Qingdao 266580, China

[3]Normandie University, ENSICAEN, UNICAEN, CNRS, Laboratory of Catalysis and Spectrochemistry, 14000 Caen, France

‡ These two authors contributed to this work equally.

* Corresponding author. Tel: +86-532-86981812

E-mail address:*baipeng@upc.edu.cn (P. Bai)*

ABSTRACT

Perovskite-type $LaCoO_3$ catalysts were studied for cyclohexane oxidation with molecular oxygen in a solvent-free system. Catalysts with various Lanthanum to Cobalt molar ratios were prepared through a modified citric acid procedure and characterized by different techniques. Among all catalysts, the best cyclohexane conversion results (8.3%) with a K/A oil (cyclohexanone and cyclohexanol) selectivity of 90% were obtained over $LaCoO_3$ with a La to Co molar ratio of 1:1. The high catalytic activity on the perovskite-type $LaCoO_3$ catalyst was explored by experimental and theoretical methods. Density functional theory-based calculations clarified the role of La and Co ions in oxygen and cyclohexane adsorption, respectively.

The characterization results indicated that a single-phase $LaCoO_3$ perovskite with a dominance of surface Co^{3+} species and relatively high concentration of adsorbed oxygen species on the catalyst surface enhances the catalytic performance. This study presents insights into the design of a highly active, cost-effective, and green catalyst for cyclohexane partial oxidation.

Keywords: Perovskite, Cyclohexane partial oxidation, $LaCoO_3$, DFT, Structure-activity relationship

INTRODUCTION

The liquid phase partial oxidation of hydrocarbons into oxidized products is of great commercial importance in the chemical industry, especially, in the polymer and petrochemical industries.[1] Cyclohexane partial oxidation is a commercially desirable reaction for the oxidation of petroleum-based feedstock processes, for which the target products, cyclohexanone ($C_6H_{10}O$) and cyclohexanol ($C_6H_{11}OH$) also referred to as K/A oil,[2] are crucial intermediates for the production of Nylon-6 and Nylon-66.

For cyclohexane partial oxidation, heterogeneous transition metal catalysts have been widely studied, among which cobalt-based catalysts are the foremost investigated, due to the proven performance of cobalt salts in the industrial homogeneous process,, where the conversion of cyclohexane is controlled to be around 4% in order to inhibit the side-reactions, commonly having a K/A oil selectivity of about 80%.[2] Cobalt has been applied either as oxides or immobilized on different supports, such as oxides[3], molecular sieves,[4] MOFs,[5-6] and carbon-based supports.[7]

These catalysts, however, typically necessitate the use of an initiator, additional organic solvent, as well as *tert*-butylhydroperoxide (TBHP) as an oxidizing agent, leading to not only product contamination and the tedious separation procedure but also critical environmental issues.

For environmental and economic reasons, solvent-free systems that utilize molecular oxygen as an oxidizing agent (no extra solvent besides cyclohexane) are attractive for modern commercial applications. In addition, a more environmentally-friendly process would be achieved if a low-cost heterogeneous catalyst was developed to replace the homogeneous one. Co-TUD catalysts with different Si/Co ratios (10–100) have been prepared and applied for the aerobic cyclohexane oxidation, yielding a selectivity of 90.4% to mono-oxygenates with a low cyclohexane conversion (3.8%) under 15 bars.[8] Previous studies indicate that a combination of two or more elements can

significantly improve the catalyst activity.[9-12] For example, Xie et al. incorporated cobalt into mixed metal oxide catalysts to enhance the catalytic performance in the selective oxidation of ethylbenzene.[10]

As an interesting catalytic material, transition-metal oxides with perovskite-type structures bear intrinsic advantages, such as structural simplicity and flexibility, high hydrothermal stability, high poisoning resistance, cost-effectiveness, and excellent oxygen mobility, which received wide attention and has been considered as green catalyst, especially in oxidation reactions.[13-15] The redox behavior of these ABO_3 type perovskites is essentially governed by B-site transition metal cation properties and the role of A-site cations is usually secondary. For example, Futai and colleagues[16] conducted an H_2-TPR analysis on the A-site substitution of $ACoO_3$ compounds by rare earth metals (A = La, Pr, Nd, Sm, Eu, Gd, Tb, Dy). All compounds exhibited two reduction peaks assigned to the reduction of cobalt ions. The oxygen mobility studies by O_2-TPD indicate that the surface of Lanthanum-based perovskites is capable of adsorbing oxygen and desorbing active oxygen species.[17] The liberated active oxygen species have a fundamental role in fueling the reaction. Zhang et al.[18] synthesised a series of $La_{1-x}Ce_xFeO_3$ catalysts which exhibited a high sulphur selectivity (almost 100%) and low activation energy in the selective oxidation of H_2S. It was found that with cerium incorporation, more Fe^{3+} and Ce^{4+} ions participated in the oxidation reaction, improving the reducibility and lattice oxygen mobility of the catalyst. A non-stoichiometric $LaMnO_3$ perovskite-type catalyst was tested in NO oxidation and results indicated that a lower La content in A site induced the conversion of Mn(III) into Mn(IV) for charge balance and structural stability. Compared to the stoichiometric $LaMnO_3$, the nonstoichiometric $La_{0.9}MnO_3$ catalyst exhibited a higher activity in NO oxidation due to the easily regenerated oxygen associated with Mn(IV).[19] In another report,[20] the effect of M-doped (M = Mn, Fe, and Co) single-phased

$La_{0.08}Sr_{0.92}Ti_{1-x}M_xO_{3-\delta}$ on the activity of methane oxidation was investigated. Fe and Co-doped catalysts demonstrated excellent performance associated with the high atomic ratios of Fe^{3+}/Fe^{4+} and Co^{3+}/Co^{4+} in comparison to Mn^{3+}/Mn^{4+} in the Mn-doped sample. Although the perovskite materials exhibit a high potential in the oxidation reaction, there is no report on the application of such materials in partial oxidation of cyclohexane so far.

Intrigued by the inherent advantages of perovskite in oxidation reactions, a perovskite-type Lanthanum Cobalt oxide ($LaCoO_3$) was prepared and tested in the solvent-free partial oxidation of cyclohexane with molecular oxygen as an oxidant in this work. $LaCoO_3$ perovskites with different La to Co molar ratios were synthesized and characterized by a variety of techniques. The nature of active sites in the perovskites for cyclohexane oxidation were clarified by combining the experimental and theoretical calculation results.

EXPERIMENTAL SECTION

Chemicals

$La(NO_3)_3 \cdot 6H_2O$ **,** $Co(NO_3)_2 \cdot 6H_2O$ **,** NaOH , $C_6H_8O_7 \cdot H_2O$ **,** cyclohexane (99.99%) and absolute ethanol (99.98%), all obtained from Sinopharm Chemical company, were used as received without further purification.

Catalyst Preparation

The catalysts were prepared by a modified citric acid method using citric acid as the chelating agent. Lanthanum nitrate and cobalt nitrate were dissolved in water with certain molar ratios. The above solution was added dropwise to a sodium hydroxide solution. After two hours of constant stirring to ensure complete precipitation, the sample was filtered and washed to remove the residue ions. The obtained wet cake was added to a citric acid solution and stirred at room temperature for

12 hours to ensure the complete complexation of the metal hydroxides. The molar ratio of citric acid to total metal ions was 1.2 to 1. Then, the mixture was dried at 110^{o}C for 24 h. Finally, the obtained powder was annealed in air at 750^{o}C for 4 h. According to the molar ratio of La: Co, the resultant samples were named as $La_1Co_{0.8}O_3$, $La_1Co_1O_3$, and $La_{0.8}Co_1O_3$, respectively. The pure metal oxides were prepared through the same procedure and named as La_2O_3 and Co_3O_4 for lanthanum and cobalt oxides, respectively.

Characterization

X-ray diffraction (XRD) patterns of the samples were reported on a Bruker AXS D8 Advance X-ray diffractometer fitted by a LynxEye detector with 40 kV and 40 mA working Cu-$K\alpha$ radiation (λ=1.5406 Å). Diffraction patterns were collected in a 2θ range of 15° to 75° with a 0.02° step size at a scan rate of 2°/min. The average crystallite size was calculated by Debye-Scherrer's formula. Diffrac Eva v4.3 software was employed for phase identification and Topas v6 package for the Rietveld refinement of the crystalline structures. A fifth-order Chebychev background model and Thompson-Cox-Hastings pseudo-Voigt peak model were used to fit the diffraction patterns. The atomic positions were determined for each material and the thermal parameter was constrained for all atoms. From the diffractograms, the crystallite size (D) of crystals were calculated using the Debye-Scherrer equation;

$$D = \frac{K\lambda}{\beta \cos\theta} \qquad (1)$$

where K is a unit cell geometry dependent constant, which usually takes a value of about 0.9, λ is the wavelength of the X-ray source used in XRD, β is the width of the observed diffraction line at its half-intensity maximum in radian and θ is the Bragg peak angle[14]. A Bruker Vertex 70V Tensor 27 spectrometer at 4 cm^{-1} resolution with 32 scans was utilized to perform Fourier transform infrared (FT-IR) spectroscopy in KBr media at room temperature. The FT-IR spectra were

measured in the 4000–400 cm^{-1} region. Nitrogen physisorption isotherms were recorded at 77 K using a Micromeritics ASAP2020 gas adsorption analyser. Each sample was degassed at 300 °C for 3 h prior to the adsorption. According to the Brunauer-Emmett-Teller (BET) formula, the specific surface area was determined from the adsorption branch in the P/P_o range of 0.05 to 0.30. The pore size distribution was determined from the desorption branch analysis of the N_2 isotherm using the BJH (Barrett-Joyner-Halenda) method. Surface morphology and elemental composition were determined by scanning electron microscopy (SEM, JSM-7600F; JEOL, USA) equipped with an energy-dispersive X-ray spectroscopy (EDX). A JEOL JEM-1210 microscope working at 113-115 kV and fitted with an Olympus Megaview G2 camera was used to obtain transmission electron microscopy (TEM) images. In order to examine the reduction behavior of the catalysts, H_2-temperature programmed reduction (H_2-TPR) experiments were performed on a chemisorption apparatus (Micromeritics AutoChem II 2920). The sample (100 mg) was typically pre-treated for 1 h under an Ar stream (30 mL / min) at 300 °C to eliminate moisture and impurities. The system was then cooled to 50 °C, and reduced by introducing a 10 vol% H_2/Ar stream (30 mL/min). Afterwards, the temperature was increased linearly from 100 °C to 900 °C at 10 °C/min, and the thermal conductivity detector (TCD) signal was recorded. The evaluation of X-ray photoelectron spectroscopy (XPS) was carried out on a Thermo Fisher Scientific spectrometer fitted with an Al electrode as an anode at an electron kinetic energy of 1486.6 eV. The spectra were calibrated with C 1s binding energy (284.5 eV) as an internal standard. The results were analysed by CasaXPS software using Shirley and tougaard backgrounds for oxygen and cobalt, respectively. The room temperature X-band electronic paramagnetic resonance (EPR) spectra were collected on a JEOL JESFA200 ESR spectrometer.

Catalytic Evaluation

The catalysts' performance in the cyclohexane partial oxidation was evaluated in a 100 mL stainless steel reactor furnished with a magnetic stirrer. In a standard reaction, 7.56 mL of cyclohexane and 50 mg of catalyst were added into the reactor. The reactor was heated to 150 ^{o}C after oxygen purging and charged with 0.8 MPa of O_2 for 1 hour under stirring. After the reaction, the mixture was diluted with a certain amount of ethanol to dissolve the by-products, and then the catalyst was removed by a micro-filtration. The products were identified by GC-MS (Agilent 7890A-5975C) with a Restek Stabilwax-DA capillary column. The liquid products were analyzed by a Perkin-ElmerClarus 500 gas chromatograph equipped with a capillary column packed with cross-bond PEG treated with nitro-terephthalic acid (30*0.32*0.25) and a FID detector. Pentanol was used as the internal standard. The regeneration was carried out by separating the spent catalyst from the reaction mixture through centrifugation, dried at 100 ^{o}C in an oven for 5 hours, calcined at 550 ^{o}C for 4 hours, and then charged for the further run under the same reaction conditions. Due to the loss of catalyst, the amount of cyclohexane fed for the following cycles was reduced accordingly.

Theoretical Calculation

Density functional theory (DFT) calculations were implemented using the DMol^3 program of Materials Studio 2018 software package. For geometry optimization steps, spin unrestricted calculations were performed using the Perdew−Burke−Ernzerhof (PBE) within the generalized gradient approximation (GGA) method to describe the exchange-correlation functional. Double numerical basis sets with polarization functions (DNP) and DFT semi-core pseudopotential (DSSP) were utilized for all calculations. After convergence assessment, a 3 × 3 × 1 Monkhorst−Pack k-point mesh for the Brillouin zone sampling at a global orbital cutoff of 5.0 Å was employed. The convergence specifications for optimal geometry concerning energy, force, and displacement were

set as 2×10^{-5} Ha, 4×10^{-3} Ha/Å, and 5×10^{-3} Å, respectively. The rhombohedral $LaCoO_3$ unit cell and its primitive cell structure were extracted from the Materials Project database. Based on XRD results, $LaCoO_3$ (1 1 0) slab was cleaved and a vacuum region of 15 Å applied to lessen interactions between periodic images. The slab-bottom three layers were fixed to describe the bulk. For oxygen and cyclohexane adsorption studies, the adsorption energy (E_{ads}) was computed from the following formula:

$$E_{ads} = E_{surf-ads} - E_{surf} - E_m \qquad (2)$$

where $E_{surf-ads}$ refers to the total energy of the surface with adsorbed oxygen/cyclohexane, E_{sub} and E_m are the total energy of clean surface and free molecular oxygen/cyclohexane, respectively.

RESULTS AND DISCUSSION

Crystalline Structure

The XRD patterns of La_2O_3, $La_1Co_{0.8}O_3$, $La_1Co_1O_3$, $La_{0.8}Co_1O_3$, and Co_3O_4 catalysts are presented in Figure 1 and their structural compositions generated by the Rietveld refinement method are summarized in Table 1. In Figure 1, no other phase was observed on sample $La_1Co_1O_3$, except rhombohedral perovskite phase (*R*-3C) of $LaCoO_3$, whereas obvious diffraction peaks of La_2O_3 and Co_3O_4 phases were detected on $La_1Co_{0.8}O_3$ and $La_{0.8}Co_1O_3$, respectively. The refinement results confirmed a pure rhombohedral perovskite $LaCoO_3$ phase on catalyst $La_1Co_1O_3$, while hexagonal La_2O_3 phase (P63/mmc) and cubic Co_3O_4 phase (Fd-3m) were observed on catalysts $La_1Co_{0.8}O_3$ and $La_{0.8}Co_1O_3$, respectively, besides the *R*-3C perovskite phase. The proportion of different phases on catalysts $La_1Co_{0.8}O_3$ and $La_{0.8}Co_1O_3$ were quantified as $La_2O_3/LaCoO_3$ (P63/mmc: R-3C) =23: 77 and $Co_3O_4/LaCoO_3$ (Fd-3m: R-3C) = 20: 80, respectively (as listed in Table S1).

Furthermore, the refined atomic positions, bond-angle, and bond length of $La_1Co_1O_3$ are shown in Table S2. For this sample, the calculated Co–O–Co bond angle were found to be 165º, and the six Co–O bonds have average lengths of 1.931 Aº, which are in agreement with literature results.[21-22] No obvious lattice parameter variation of the perovskite phase was observed with the different La/Co molar ratios. The average crystallite sizes of different catalysts were calculated by Debye-Scherrer equation and the results are shown in Table 1. The mean crystallite sizes of $La_1Co_1O_3$, La_2O_3, and Co_3O_4 were estimated as 21.8, 40.4, and 56.0 nm, respectively. However, the mean crystallite sizes of catalysts $La_1Co_{0.8}O_3$ and $La_{0.8}Co_1O_3$ were between those of $LaCoO_3$ and their respective metal oxide, showing consistency with refinement results. It was noted that for the pure La_2O_3 sample, La_2O_3 phase was unstable and easily converted into $La(OH)_3$ phase within 2 hours

of exposure to air as illustrated by XRD patterns (Figure S1). The newly generated XRD peaks at $2\theta = 23.5^{o}$ and 24.5^{o} are due to the $La(OH)_3$ phase.[23-24] However, this phenomenon disappeared after formation of $LaCoO_3$ phase, indicating the formation of perovskite rhombohedral structure led to a higher stability.

The FT-IR spectra of La_2O_3, $La_1Co_{0.8}O_3$, $La_1Co_1O_3$, $La_{0.8}Co_1O_3$, and Co_3O_4 are displayed in Figure 2. The presence of different functional groups originating from the hydroxide and carbonates[25] was observed on sample La_2O_3, which was attributed to its hygroscopicity and basicity. Water and atmospheric CO_2 are easily adsorbed on the surface of La_2O_3 under ambient conditions, leading to the formation of hydroxides, chemisorbed surface carbonates, and bicarbonates species.[23-24] The sharp peak observed at 3607 cm^{-1} was ascribed to the bulk hydroxyl groups from $La(OH)_3$.[23] Generally, the bands appearing around 3435 cm^{-1} and 1629 cm^{-1} corresponded to O-H stretching and bending vibration of adsorbed water molecules.[26] Two bands around 1467 cm^{-1} and 1381 cm^{-1} were detected on sample La_2O_3 which are attributed to the presence of carbonate or bicarbonate species.[24] The intensity of these two peaks reduced with the decrease of La/Co ratio on catalyst $La_1Co_{0.8}O_3$ and $La_1Co_1O_3$, and eventually diminished on sample $La_{0.8}Co_1O_3$. The fingerprint band around 423 cm^{-1} was assigned to La-O stretching vibration while the bands at 555 and 595 cm^{-1} were due to the Co-O stretching vibration in CoO_6 octahedra of perovskite $LaCoO_3$. The presence of these three peaks confirmed the formation of perovskite phase $LaCoO_3$ in samples $La_1Co_{0.8}O_3$, $La_1Co_1O_3$, and $La_{0.8}Co_1O_3$.[15, 27] The shoulder peak (555 cm^{-1}) signifies a lower symmetry structure such as the rhombohedra due to the asymmetrical lengthening of the Co-O bond in the structure's CoO_6 octahedra.[15] For the Co_3O_4 material, the distinguished sharp peaks at 571 and 669 cm^{-1} are associated with the OB_3 and the ABO_3 vibrations in the spinel lattice, respectively, where B denotes Co^{3+} in an octahedral

coordination and A denotes the Co^{2+} in a tetrahedral coordination,[28] indicating the presence of both Co^{2+} and Co^{3+} species on sample Co_3O_4. The peak intensity at 669 cm^{-1} corresponding to Co^{2+} species gradually reduced with the increase of La/Co ratio and disappeared on catalyst $La_1Co_1O_3$. Furthermore, no other characteristic bands between 1000 cm^{-1} and 3500 cm^{-1}, suggesting the absence of impurities such as CoOOH and $Co(OH)_2$ in the sample.[29]

Textural Properties and Microstructures

The N_2 adsorption-desorption isotherms and their corresponding BJH pore size distribution curves of the samples are presented in Figure S2(a) and Figure S2(b), respectively. All samples show a type-II sorption isotherm with a macroporous or nonporous structure.[30] Distinct H-3 hysteresis loops in the high relative pressure range of 0.8 ~ 1.0 were observed.[31] The absence of adsorption plateaus at relative pressures close to unity could be related to the existence of gaps created by pile-up of the nanoparticles, an indication that the pore size distribution extends to the macropore range clearly evidenced in the pore size distribution plots. The specific surface area, pore size, and pore volume are summarized in Table 1. The specific surface areas for the samples are low due to the high calcination temperature (750 ^oC) and no significant difference was observed on these samples.

The morphology and elemental distribution of catalysts La_2O_3, $La_1Co_{0.8}O_3$, $La_1Co_1O_3$, $La_{0.8}Co_1O_3$, and Co_3O_4 were revealed by SEM with EDX mapping as shown in Figure 3 and Figure S3. Nanosized particle aggregates were observed on all catalysts. For catalyst $La_1Co_1O_3$, the nearly spherical nanoparticles can be clearly observed with the sizes ranging from 60 to 180 nm. The color-coded EDX mapping (Inset of Figure 3) revealed a homogeneous distribution of La: Co: O elements in sample $La_1Co_1O_3$ with an atomic ratio of nearly 1:1:2.7, indicating the formation of pure perovskite phase. Figure S3 shows the EDX composition scans for La_2O_3, $La_1Co_{0.8}O_3$,

$La_{0.8}Co_1O_3$, and Co_3O_4. The atomic ratios are in agreement with nominal ratios, i.e. 2:3.1, 1:0.7:2.3, 0.7:1:2.8 and 3:4.1 for La_2O_3, $La_1Co_{0.8}O_3$, $La_{0.8}Co_1O_3$ and Co_3O_4, respectively.

TEM technique was used to further characterize the morphology and microstructure of catalyst $La_1Co_1O_3$. As shown in Figure 4, the lattice fringes could be clearly observed from the high-magnification image with a spacing of d = 0.268 ± 0.01 nm, corresponding to the (104) plane of the rhombohedral $LaCoO_3$ structure. The selected area electron diffraction (SAED) pattern of $La_1Co_1O_3$ sample (Inset of Figure 4) shows spotty ring patterns revealing a polycrystalline structure. The diffraction rings from SAED patterns were measured to be the (012), (104), and (024) planes, indicating the rhombohedral $LaCoO_3$ structure as well. These results are consistent with the XRD analysis.

Reduction Properties

In order to examine the redox ability of La_2O_3, $La_1Co_{0.8}O_3$, $La_1Co_1O_3$, $La_{0.8}Co_1O_3$, and Co_3O_4, H_2-TPR experiments were performed as shown in Figure 5. For catalyst $La_1Co_1O_3$, the hydrogen consumption involved two reduction regions located between 250 - 450 °C and 480 - 650 °C, which correspond to the reduction of Co^{3+} to Co^{2+} and Co^{2+} to Co^0, respectively.[32-33] In the lower temperature region, the main peak at 360 °C was ascribed to the reduction of surface Co^{3+} to Co^{2+} and a shoulder peak at 393 °C to the reduction of bulk Co^{3+} to Co^{2+} ions.[33] With the decrease of La to Co ratio, the first two reduction peaks of $La_{0.8}Co_1O_3$ shifted to lower temperatures. The variation was associated with the presence of dispersed Co_3O_4 particles in the perovskite phase which could be easily reduced. This is confirmed by the reduction peak of pure Co_3O_4 sample showing a complete reduction of Co^{3+} to Co^0 within the lowest temperature range of 250 - 480 °C among all catalysts. The influence of lanthanum on the reduction property of catalysts is explicitly noticeable as the ratio of lanthanum to cobalt increases, that is, the reduction temperature increased

with the increase of La to Co ratio. This is probably due to the strong interaction between cobalt-lanthanum ions and the segregation of La_2O_3 species on catalyst surface which inhibit the reduction of Co species.[12, 34] No noticeable reduction peaks were detected on sample La_2O_3 since La^{3+} ions are non-reducible under this temperature.[35]

Surface Composition and Valence States

XPS analysis was conducted to explore the surface properties of the catalysts. The detailed surface atomic concentrations are listed in Table S3 and the calculated surface La/Co ratios are summarized in Table 1. As shown in Table 1, the bulk La/Co ratios measured by EDX characterization are consistent with nominal atomic ratio. However, the surface La/Co ratios on all catalysts are higher than the bulk ones, indicating the enrichment of lanthanum at the surface of perovskites which have been considered as a common observation.[36-37]

In La 3d spectra, the binding energies (BE) of La $3d_{5/2}$ are located at 833.9 and 837.6 eV, the BEs of La $3d_{3/2}$ are located at 850.4 and 854.4 eV, respectively, as shown in Figure 6. In this work, the difference between the spin-orbit splitting of the La 3d core-level for the perovskite containing samples are found to be ~16.7 eV identical to those of La_2O_3 (16.8 eV), which suggests that the La manifests as La^{3+} species for all samples.[37] However, the peaks of La 3d shift to higher BE as the lanthanum loading increases, suggesting La loses electrons, which indicated the presence of $La(OH)_3$ species.[38]

Correlating with the surface metal composition results (Table 1), it can be concluded that more La species enriched on the catalyst surface with the increase of La/Co ratio, which tends to form surface hydroxide species when exposed to water/moisture.

Figure 7 shows the XPS spectra of Co 2p, two major observed peaks with BE of 779.7 eV and 794.6 eV were assigned to Co $2p_{3/2}$ and Co $2p_{1/2}$, respectively. Deconvolution of the asymmetrical Co $2p_{2/3}$ spectrum of each catalyst yields five components at BEs of 779.3, 780.1, 781.9, 784.2, and 789.6 eV, which correspond to surface metal Co^0, Co^{3+}, $Co^{2+,}$ and two shake-up satellite peak (Sat 1 and Sat 2) species, respectively.[39-40] Recent studies on oxidation state variations of the cobalt species reveal that the shake-up peak at ~ 784.2 eV (Sat 1) show the pronounced intensity characteristic of high spin cobalt (II) species, whereas the low spin cobalt (III) states show a very weak shake-up peak at about 789.6 eV (Sat 2). As the Co content increases, a noticeable change in the high spin satellite peak can clearly be seen. By conducting an area comparison of the two fitted shakeup satellites, changes in the oxidation state of cobalt species are noted. The ratio between Sat 1 to Sat 2 generally increases with the increase of cobalt content as shown in Table 2, indicating a decrease in Co^{3+} content on the surface. The energy difference (ΔE) between the $2p_{3/2}$ and $2p_{1/2}$ peaks can be used, in addition to the satellite comparison, to analyze the changes in the state of cobalt oxidation. An energy difference of 15-15.4 eV suggests a dominant contribution of Co^{3+}, as proposed by Anantharamaiah and Joy while the ΔE ranges from 15.7 to 16.1 eV for samples rich in Co^{2+}.[40] The summarized energy differences results (ΔE in Table 2) indicate that $La_1Co_1O_3$ displayed the lowest ΔE compared to other catalysts while the highest value was found in sample Co_3O_4. This emphasizes the enrichment of Co^{2+} on the surface of sample Co_3O_4. As indicated in Table 2, the highest surface Co^{3+}/ Co_{total} ratio was observed on catalyst $La_1Co_1O_3$ and it decreases with the reduction of perovskite phase. It has been widely accepted that the valence state of the cobalt species is crucial for the catalytic activity.[41-42]

The O 1s spectra of catalysts La_2O_3, $La_1Co_{0.8}O_3$, $La_1Co_1O_3$, $La_{0.8}Co_1O_{3,}$ and Co_3O_4 are presented in Figure 8 and their relative oxygen atomic concentrations are displayed in Table 2. A satisfactory

deconvolution yielded three components located at 529.2 ± 0.5, 530.8 ± 0.5 and 532.7 ± 0.6 eV, which correspond to surface lattice oxygen (O_α), surface adsorbed oxygen (O_β) and oxygen-containing group species on the surface (O_γ) such as CO_3^{2-} or OH^-.[43-45] Generally, the results show an increase of surface oxygen species (O_β and O_γ) at the expense of the lattice oxygen O_α with the increase of lanthanum ratio in the samples, which is consistent with those reported by Bae et al.[46] The shift in binding energy positions is due to the incorporation of different elements which alter the electron density around the base element. The O_β species play a vital role in promoting the surface reactivity of an oxidation reaction since they have higher mobilities relative to the O_α species.[47] A higher O_β/O_α value usually indicates a higher oxygen vacancy density, which is believed to act as the adsorption site for the active oxygen species.[48]

The EPR spectra of $La_1Co_1O_3$ and $La_{0.8}Co_1O_3$ samples shown in Figure 9, were recorded to further understand the valence state of cobalt ion. Cobalt (III) oxidation state is diamagnetic in nature (EPR silent) while the cobalt (II) ion is paramagnetic (EPR active).[49-50] Our results demonstrate the presence of paramagnetic ions on both catalyst surfaces with a stronger peak intensity for $La_{0.8}Co_1O_3$ confirming more Co^{2+} ions[50] than in the $La_1Co_1O_3$ sample. These results are in agreement with the XPS analysis.

DFT Calculations

Oxygen and cyclohexane adsorption on the perovskite surface were investigated using density functional theory (DFT) calculations. The optimized primitive cell with lattice parameters of a = b = c = 5.393 Å and $\alpha = \beta = \gamma = 61.2^o$ was adopted for the studies. The dominant XRD perovskite phase (110), was chosen as the surface of adsorption. The 2 x 2 x 1 supercell of $LaCoO_3$ slab model along the (110) direction, consisting of six alternating layers of LaO and CoO_2 planes was used to study the adsorption behavior of molecular oxygen and cyclohexane. The CoO_2(110)-termination

with the corresponding Co-atop, O-atop, and hollow-atop sites are illustrated in Figure 10(A) and (C), respectively. Similarly, Figure 10(B) shows the LaO(110)-terminated surface. The top view exposes both La and O atoms as well as La-La bridge sites shown in Figure 10(D).

Since adsorbates prefer association with cations over oxygen anions, we studied the effect of La and Co ions on O_2 and cyclohexane adsorption.[51] Free molecular oxygen and cyclohexane ring were placed in various orientations on both surfaces as adsorbents and optimized to identify the lowest energy structures, which are shown in Figure 11 and the structural properties summarized in Table 3. As is shown, the O_2 adsorption prefers the Co-atop and hollow-atop sites for CoO_2(110) and LaO(110)-terminations, respectively.

The computed O-O bond length of free molecular oxygen was 1.225 Å, which is slightly larger than the experimental value of 1.208 Å[52] but in agreement with the previously reported value.[53] Adsorption on the CoO_2(110) and LaO(110)-terminated facets lengthens it by 0.053 and 0.169 Å, respectively. La_2O_3(001) surface also shows a higher elongation (0.089 Å) than that depicted by the cobalt perovskite surface, which suggests that molecular oxygen continuously withdraws more electrons from the La surface to the O_2-2π* orbitals creating the larger O-O bond elongation. Furthermore, the O_2 adsorption is much more energetically stable on the LaO(110)-termination (-2.04 eV) than on CoO_2(110)-termination (-0.56 eV). These results may be attributed to the difference in electronegativity between the La (1.1) and Co (1.88) ions which implies that La ions can strongly attract O_2 compared to the Co ions. The preference for La over Co surface indicates that molecular O_2 is easily activated upon adsorption on the La ion to yield O-O bond breakage which is key for the progress of the oxidation process. These computational results are in good agreement with the oxygen XPS results and that of reported literature.[54] From the orientations of the different adsorption sites considered for cyclohexane on perovskite surfaces, the obtained

results showed that cyclohexane molecule adsorbed predominantly in the chair conformation[55] for both terminations (Figure 11). The adsorption on the CoO_2-termination recorded the most stable configuration with an energy of -0.99 eV compared to LaO-termination (-0.82 eV) and the reference La_2O_3 surface (-0.73 eV). Additionally, the most significant increase for cyclohexane adsorption was from 1.104 to 1.113 Å in the longest C-H bond on the CoO_2-termination. This change was larger than the increase from 1.104 to 1.107 Å and 1.104 to 1.106 Å for the longest C-H bond on LaO-termination and La_2O_3 surfaces, respectively. The preference and elongation of cyclohexane on cobalt-perovskite surface show that the cleavage of inert C-H bond is more likely on CoO_2-termination.

Catalytic Performance

The catalytic performance of samples prepared in this work and employed for cyclohexane oxidation at 150 ^oC for 1 hour were summarised in Table 4. For the single metal oxide catalysts, Co_3O_4 exhibited a slightly higher conversion (3.9%) than its counterpart La_2O_3 (2.6%). Nevertheless, its activity was quite lower than that of perovskite containing catalysts. $La_1Co_1O_3$ was the most active among the studied catalysts achieving a conversion of 8.3%, which suggests a synergistic action between the two metals. However, as the predominant crystal phase changes from perovskite to a mixture of phases, the conversion decreases i.e. to 6.1% and 6.3% for $La_1Co_{0.8}O_3$ and $La_{0.8}Co_1O_3$, respectively, which signified that the purity of the perovskite influences the reaction. All catalysts showed good K/A oil selectivity ($\geq$ 90%) and favored cyclohexanone formation except catalyst La_2O_3 which yielded more cyclohexanol as clearly reflected by the K/A ratio.

In order to understand the stability of the perovskite catalyst during the reaction-regeneration cycles, the $La_1Co_1O_3$ catalyst was retrieved and regenerated. Figure 12 shows the

conversion/selectivity results of the regenerated $La_1Co_1O_3$ catalyst over five cycles. The regenerated $La_1Co_1O_3$ catalysts' performance was quite similar to that of the fresh catalyst and the achieved conversions are above 8.3% with target product selectivity above 86.5%. No evident deterioration in activity/selectivity of the regenerated $La_1Co_1O_3$ catalyst was observed after the five cycles. The results show that the spent catalyst was able to recover its activity after the simple calcination treatment. The XRD patterns of catalyst $La_1Co_1O_3$ before and after reaction revealed no obvious structure change (Figure S4), certified the good stability of catalyst. The relation between Co^{3+}/Co_{total}, $O_\beta/O_{\alpha,}$ and the conversion attained on different catalysts was displayed in Figure 13. For the cobalt-containing catalysts, a volcano-shape profile was observed in the cyclohexane conversion, which increased with increase in the Co^{3+}/Co_{total} ratio. $La_1Co_1O_3$ catalyst with the highest Co^{3+}/Co_{total} ratio (0.53) recorded the best conversion (8.3%) whereas Co_3O_4 (0.32) gave the least conversion (3.9%). Generally, with incorporation of La ions, the O_β/O_α increased with increment in the lanthanum loading which could be due to the difference in electronegativity between the La (1.1) and Co (1.88) ions, hence La ion possesses the ability to attract more oxygen compared to the cobalt ions. A comparison of the attained conversion results between the single-phase and mixed-phase catalysts confirmed that the presence of the perovskite phase influenced the catalyst activity. DFT calculations suggest that La^{3+} sites are more favorable for molecular oxygen adsorption/activation than the Co^{3+} sites, whereas the Co^{3+} ions prefer the adsorption of cyclohexane to foster the C-H bond activation. This trait is in good agreement with the data from the literature, where Co^{2+} is commonly recognized inactive while Co^{3+} as the active species for heterogeneous oxidation reactions.[56-57] Therefore, it can be concluded that the perovskite catalyst ($LaCoO_3$) favors the activation of C-H bond which is believed to be the rate-controlling step in cyclohexane partial oxidation[58] and the catalytic performance can be enhanced through the catalyst

design. The formation of a single-phase perovskite, leading to a prevalence of Co^{3+} and the inherent surface oxygen of lanthanum containing perovskites are responsible for the enhanced cyclohexane oxidation.

A reaction mechanism for partial oxidation of cyclohexane over the $LaCoO_3$ perovskite catalyst was proposed on the basis of experimental and theoretical studies, as shown in Scheme 1. Molecular oxygen ($O_{2\ gas}$) is activated on $LaCoO_3$ surface by chemisorption on the lanthanum surface, accompanied by the formation of activated oxygen species ($O_{2\ ads}^{-}$) while cyclohexane is activated on Co^{3+} on the catalyst surface. The activated species interact to form the cyclohexylperoxyl radical which further transforms to cyclohexyl hydroperoxide (CHHP) intermediate. Then, the CHHP decomposes to cyclohexanol and cyclohexanone which are the main products of the reaction.

CONCLUSIONS

A series of catalysts with varying lanthanum to cobalt ratios were successfully prepared using a modified citric acid approach and evaluated in cyclohexane oxidation. The obtained $LaCoO_3$ perovskite material was identified as an excellent catalyst for cyclohexane oxidation reaction, which was interpreted by correlating the catalytic activity with a variety of characterization techniques and DFT studies. Based on the XRD and FT-IR characterization data, $La_1Co_1O_3$, and Co_3O_4 samples show the presence of a single-phase while La_2O_3, $La_1Co_{0.8}O_3$, and $La_{0.8}Co_1O_3$ samples contain mixed phases. Cobalt-XPS and EPR analysis confirmed that the surface Co^{3+} species in the material increased with the purity of the perovskite phase. DFT calculations coupled with oxygen-XPS studies reveal that La ion sites are more favorable for molecular oxygen adsorption than the Co ion sites whereas cyclohexane preferred Co sites. The single-phase rhombohedral $La_1Co_1O_3$ sample exhibited the highest activity. The excellent catalytic performance

of $LaCoO_3$ perovskite under mild reaction conditions could be attributed to the dominance of Co^{3+} ions which aid in cyclohexane C-H bond activation and the presence of relatively abundant adsorbed oxygen species on the catalyst due to the amplified O_2 adsorption lanthanum surface. These findings could shed light on the design of an environmentally-friendly, low-cost, and highly active perovskite catalyst for cyclohexane oxidation.

ASSOCIATED CONTENT

Supporting Information

The Supporting Information is available free of charge at

XRD patterns for La_2O_3**,** N_2 adsorption-desorption isotherms and pore size distribution, EDX mappings**,** surface atomic concentrations measured by XPS, structural parameters and refined unit cell lattice parameters.

AUTHOR INFORMATION

Corresponding Author

Peng Bai — *State Key Laboratory of Heavy Oil Processing, CNPC Key Laboratory of Catalysis, College of Chemical Engineering, China University of Petroleum (East China), Qingdao 266580, China*； E-mail address:*baipeng@upc.edu.cn*;

Authors

Pingping Wu — *State Key Laboratory of Heavy Oil Processing, CNPC Key Laboratory of Catalysis, College of Chemical Engineering, China University of Petroleum (East China), Qingdao 266580, China;*

Edgar Muhumuza — *State Key Laboratory of Heavy Oil Processing, CNPC Key Laboratory of Catalysis, College of Chemical Engineering, China University of Petroleum (East China),*

Qingdao 266580, China;

Tian Nan — *State Key Laboratory of Heavy Oil Processing, CNPC Key Laboratory of Catalysis, College of Chemical Engineering, China University of Petroleum (East China), Qingdao 266580, China;*

Lianming Zhao — *School of Materials Science and Engineering, Institute of Advanced Materials, China University of Petroleum (East China), Qingdao 266580, China;*

Svetlana Mintova — *State Key Laboratory of Heavy Oil Processing, CNPC Key Laboratory of Catalysis, College of Chemical Engineering, China University of Petroleum (East China), Qingdao 266580, China; Normandie University, ENSICAEN, UNICAEN, CNRS, Laboratory of Catalysis and Spectrochemistry, 14000 Caen, France;*

Zifeng Yan — *State Key Laboratory of Heavy Oil Processing, CNPC Key Laboratory of Catalysis, College of Chemical Engineering, China University of Petroleum (East China), Qingdao 266580, China;*

Author Contributions

ǂ Pingping Wu and Edgar Muhumuza contributed equally to this work.

Notes

The authors declare no competing financial interest.

ACKNOWLEDGEMENTS

This work was supported by National Natural Science Foundation of China (51601223, 21991091), the National Key Technologies R & D program of China (2018YFE0118200), Shandong Provincial Natural Science Foundation (ZR2017MB003), PetroChina Innovation Foundation (2018D-5007-0504), the Fundamental Research Funds for the Central Universities (17CX05018, 17CX02056, 19CX05001A) and the Sino-French International Laboratory (LIA)

“Zeolites”. E. M. would like to appreciate the financial support from the China Scholarship Council.

REFERENCES

(1) Liu, X.; He, J.; Yang, L.; Wang, Y.; Zhang, S.; Wang, W.; Wang, J. Liquid-phase oxidation of cyclohexane to cyclohexanone over cobalt-doped SBA-3. *Catal. Commun.* **2010**, *11*, 710-714.

(2) Alshaheri, A. A.; Tahir, M. I. M.; Rahman, M. B. A.; Ravoof, T. B.; Saleh, T. A. Catalytic oxidation of cyclohexane using transition metal complexes of dithiocarbazate Schiff base. *Chem. Eng. J.* **2017**, *327*, 423-430.

(3) Zhou, L.; Xu, J.; Miao, H.; Wang, F.; Li, X. Catalytic oxidation of cyclohexane to cyclohexanol and cyclohexanone over Co_3O_4 nanocrystals with molecular oxygen. *Appl. Catal., A* **2005**, *292*, 223-228.

(4) Kondo, J.; Yamazaki, H.; Yokoi, T.; Tatsumi, T. Mechanisms of reactions of methoxy species with benzene and cyclohexane over H-ZSM-5 zeolites. *Catal. Sci. Technol.* **2015**, *5*, 3598-3602.

(5) Shi, D.; Ming, Z.; Wu, Q.; Lai, T.; Zheng, K.; He, C.; Zhao, J. A novel photosensitizing decatungstate-based MOF: Synthesis and photocatalytic oxidation of cyclohexane with molecular oxygen. *Inorg. Chem. Commun.* **2019**, *100*, 125-128.

(6) Li, L.; Yang, Q.; Chen, S.; Hou, X.; Liu, B.; Lu, J.; Jiang, H.-L. Boosting selective oxidation of cyclohexane over a metal–organic framework by hydrophobicity engineering of pore walls. *Chem. Commun.* **2017,** *53*, 10026-10029.

(7) Andrade, M. A.; Mestre, A. S.; Carvalho, A. P.; Pombeiro, A. J.; Martins, L. M. The role of nanoporous carbon materials in catalytic cyclohexane oxidation. *Catal. Today* **2019,** https://doi.org/10.1016/j.cattod.2019.07.036.

(8) Ramanathan, A.; Hamdy, M. S.; Parton, R.; Maschmeyer, T.; Jansen, J. C.; Hanefeld, U. Co-TUD-1 catalysed aerobic oxidation of cyclohexane. *Appl. Catal., A* **2009**, *355*, 78-82.

(9) Zhang, J.; Tan, D.; Meng, Q.; Weng, X.; Wu, Z. Structural modification of $LaCoO_3$ perovskite for oxidation reactions: The synergistic effect of Ca^{2+} and Mg^{2+} co-substitution on phase formation and catalytic performance. *Appl. Catal., B* **2015**, *172-173*, 18-26.

(10) Xie, R.; Fan, G.; Yang, L.; Li, F. Hierarchical flower-like Co–Cu mixed metal oxide microspheres as highly efficient catalysts for selective oxidation of ethylbenzene. *Chem. Eng. J.* **2016**, *288*, 169-178.

(11) Konsolakis, M.; Carabineiro, S. A. C.; Marnellos, G. E.; Asad, M. F.; Soares, O. S. G. P.; Pereira, M. F. R.; Órfão, J. J. M.; Figueiredo, J. L. Effect of cobalt loading on the solid state properties and ethyl acetate oxidation performance of cobalt-cerium mixed oxides. *J. Colloid Interf. Sci.* **2017**, *496*, 141-149.

(12) Jiao, G.; Ding, Y.; Zhu, H.; Li, X.; Li, J.; Lin, R.; Dong, W.; Gong, L.; Pei, Y.; Lu, Y. Effect of La_2O_3 doping on syntheses of C_1–C_{18} mixed linear α-alcohols from syngas over the Co/AC catalysts. *Appl. Catal., A* **2009**, *364*, 137-142.

(13) Liu, T.; Yao, Y.; Wei, L.; Shi, Z.; Han, L.; Yuan, H.; Li, B.; Dong, L.; Wang, F.; Sun, C. Preparation and evaluation of copper–manganese oxide as a high-efficiency catalyst for CO oxidation and NO reduction by CO. *J. Phys. Chem. C* **2017**, *121*, 12757-12770.

(14) Chagas, C. A.; Toniolo, F. S.; Magalhaes, R. N. S.; Schmal, M. Alumina-supported $LaCoO_3$ perovskite for selective CO oxidation (SELOX). *Int. J. Hydrogen Energy* **2012**, *37*, 5022-5031.

(15) Phadtare, D.; Kondawar, S.; Athawale, A.; Rode, C. Crystalline $LaCoO_3$ perovskite as a novel catalyst for glycerol transesterification. *Mol. Catal.* **2019**, *475*, 110496.

(16) Futai, M.; Yonghua, C. Characterization of perovskite-type oxide catalysts $RECoO_3$ by TPR. *React. Kinet. Catal. Lett.* **1986**, *31*, 47-54.

(17) Baiker, A.; Marti, P. E.; Keusch, P.; Fritsch, E.; Reller, A. Influence of the A-site cation in $ACoO_3$ (A = La, Pr, Nd, and Gd) perovskite-type oxides on catalytic activity for methane combustion. *J. Catal.* **1994**, *146*, 268-276.

(18) Zhang, F.; Zhang, X.; Jiang, G.; Li, N.; Hao, Z.; Qu, S. H_2S selective catalytic oxidation over Ce substituted $La_{1-x}Ce_xFeO_3$ perovskite oxides catalyst. *Chem. Eng. J.* **2018**, *348*, 831-839.

(19) Chen, J.; Shen, M.; Wang, X.; Qi, G.; Wang, J.; Li, W. The influence of nonstoichiometry on $LaMnO_3$ perovskite for catalytic NO oxidation. *Appl. Catal., B* **2013**, *134-135*, 251-257.

(20) Yoon, J. S.; Lim, Y.-S.; Choi, B. H.; Hwang, H. J. Catalytic activity of perovskite-type doped $La_{0.08}Sr_{0.92}Ti_{1-x}M_xO_{3-\delta}$ (M = Mn, Fe, and Co) oxides for methane oxidation. *Int. J. Hydrogen Energy* **2014**, *39*, 7955-7962.

(21) Prakash, R.; Shukla, R.; Nehla, P.; Dhaka, A.; Dhaka, R. Tuning ferromagnetism and spin state in $La_{(1-x)}A_xCoO_3$ (A= Sr, Ca) nanoparticles. *J. Alloys Compd.* **2018**, *764*, 379-386.

(22) Øygarden, V.; Lein, H. L.; Grande, T. Structure, thermal expansion and electrical conductivity of Nb-substituted $LaCoO_3$. *J. Solid State Chem.* **2012**, *192*, 246-254.

(23) Lee, S.; Jang, S.; Kang, J.-G.; Sohn, Y. Luminescent Eu(III) and Tb(III) activator ions in $La(OH)_3$ and La_2O_3 nanowire matrices. *Mater. Sci. Eng., B* **2015**, *201*, 35-44.

(24) Kang, J.-G.; Kim, Y.-I.; Cho, D. W.; Sohn, Y. Synthesis and physicochemical properties of $La(OH)_3$ and La_2O_3 nanostructures. *Mater. Sci. Semicond. Process.* **2015**, *40*, 737-743.

(25) Gangwar, B. P.; Palakollu, V.; Singh, A.; Kanvah, S.; Sharma, S. Combustion synthesized La_2O_3 and $La(OH)_3$: Recyclable catalytic activity towards Knoevenagel and Hantzsch reactions. *RSC Adv.* **2014**, *4*, 55407-55416.

(26) Chumakova, V.; Marikutsa, A.; Rumyantseva, M.; Fasquelle, D.; Gaskov, A. Nanocrystalline $LaCoO_3$ modified by Ag nanoparticles with improved sensitivity to H_2S. *Sens. Actuators, B* **2019**, *296*, 126661.

(27) Zhou, C.; Feng, Z.; Zhang, Y.; Hu, L.; Chen, R.; Shan, B.; Yin, H.; Wang, W. G.; Huang, A. Enhanced catalytic activity for NO oxidation over Ba doped $LaCoO_3$ catalyst. *Rsc Adv.* **2015**, *5*, 28054-28059.

(28) Adhikari, H.; Ghimire, M.; Ranaweera, C. K.; Bhoyate, S.; Gupta, R. K.; Alam, J.; Mishra, S. R. Synthesis and electrochemical performance of hydrothermally synthesized Co_3O_4 nanostructured particles in presence of urea. *J. Alloys Compd.* **2017**, *708*, 628-638.

(29) Fu, W.; Long, L.; Wang, M.; Yao, Y.; Wei, N.; Yan, M.; Yin, G.; Liao, X.; Huang, Z.; Chen, X. Pine needle β-$Co(OH)_2$ grown on Ni foam substrate for high specific capacitance and good cycling stability as advanced electrochemical pseudocapacitor materials. *J. Alloys Compd.* **2015**, *631*, 82-85.

(30) Maity, A.; Ghosh, A.; Majumder, S. B. Engineered spinel–perovskite composite sensor for selective carbon monoxide gas sensing. *Sens. Actuators, B* **2016**, *225*, 128-140.

(31) Thommes, M. Physical adsorption characterization of nanoporous materials. *Chem. Ing. Tech.* **2010**, *82*, 1059-1073.

(32) Li, H.; Yu, K.; Wan, C.; Zhu, J.; Li, X.; Tong, S.; Zhao, Y. Comparison of the nickel addition patterns on the catalytic performances of $LaCoO_3$ for low-temperature CO oxidation. *Catal. Today* **2017**, *281*, 534-541.

(33) Luo, Y.; Wang, K.; Zuo, J.; Qian, Q.; Xu, Y.; Liu, X.; Xue, H.; Chen, Q. Enhanced activity for total benzene oxidation over SBA-15 assisted electrospun $LaCoO_3$. *Mol. Catal.* **2017**, *436*, 259-266.

(34) Brabant, C.; Khodakov, A.; Griboval-Constant, A. Promotion of lanthanum-supported cobalt-based catalysts for the Fischer–Tropsch reaction. *Comptes Rendus Chimie.* **2017**, *20*, 40-46.

(35) Pandey, A.; Jain, G.; Vyas, D.; Irusta, S.; Sharma, S. Nonreducible, basic La_2O_3 to reducible, acidic $La_{2-x}Sb_xO_3$ with significant oxygen storage capacity, lower band gap, and effect on the catalytic activity. *J. Phys. Chem. C* **2017**, *121*, 481-489.

(36) Gupta, S.; Singh, P. Nickel and titanium doubly doped lanthanum strontium chromite for high temperature electrochemical devices. *J. Power Sources* **2016**, *306*, 801-811.

(37) Haynes, D. J.; Shekhawat, D.; Berry, D. A.; Zondlo, J.; Roy, A.; Spivey, J. J. Characterization of calcination temperature on a Ni-substituted lanthanum-strontium-zirconate pyrochlore. *Ceram. Int.* **2017**, *43*, 16744-16752.

(38) Sunding, M.; Hadidi, K.; Diplas, S.; Løvvik, O.; Norby, T.; Gunnæs, A. XPS characterisation of in situ treated lanthanum oxide and hydroxide using tailored charge referencing and peak fitting procedures. *J. Electron Spectrosc. Relat. Phenom.* **2011**, *184*, 399-409.

(39) Biesinger, M. C.; Payne, B. P.; Grosvenor, A. P.; Lau, L. W.; Gerson, A. R.; Smart, R. S. C. Resolving surface chemical states in XPS analysis of first row transition metals, oxides and hydroxides: Cr, Mn, Fe, Co and Ni. *Appl. Surf. Sci.* **2011**, *257*, 2717-2730.

(40) Anke, S.; Bendt, G.; Sinev, I.; Hajiyani, H.; Antoni, H.; Zegkinoglou, I.; Jeon, H.; Pentcheva, R.; Roldan Cuenya, B.; Schulz, S. Selective 2-Propanol Oxidation over Unsupported Co3O4 Spinel Nanoparticles: Mechanistic Insights into Aerobic Oxidation of Alcohols. *ACS Catal.* **2019**, *9*, 5974–5985.

(41) Rodionova, L. I.; Smirnov, A. V.; Borisova, N. E.; Khrustalev, V. N.; Moiseeva, A. A.; Grünert, W. Binuclear cobalt complex with Schiff base ligand: Synthesis, characterization and catalytic properties in partial oxidation of cyclohexane. *Inorg. Chim. Acta* **2012**, *392*, 221-228.

(42) Wang, F.; Shen, Y.; Huang, H. Polymer nanofilm-coated Co-Mn oxide nanoparticle catalysts for trans-membrane CO oxidation at 50° C under moisture-rich conditions. *ACS Appl. Nano Mater.* **2020**, 3, 4187–4196.

(43) Wu, L.; Li, Y.; Li, S.; Li, Z.; Tang, G.; Qi, W.; Xue, L.; Ge, X.; Ding, L. Method for estimating ionicities of oxides using O1s photoelectron spectra. *AIP Adv.* **2015,** *5*, 097210.

(44) Liu, L.; Sun, J.; Ding, J.; Zhang, Y.; Sun, T.; Jia, J. Highly active $Mn_{3-x}Fe_xO_4$ spinel with defects for toluene mineralization: Insights into regulation of the oxygen vacancy and active metals. *Inorg. Chem.* **2019**, 58, 13241–13249.

(45) Liu, L.; Li, J.; Zhang, H.; Li, L.; Zhou, P.; Meng, X.; Guo, M.; Jia, J.; Sun, T. In situ fabrication of highly active γ-MnO_2/$SmMnO_3$ catalyst for deep catalytic oxidation of gaseous benzene, ethylbenzene, toluene, and o-xylene. *J. Hazard. Mater.* **2019**, *362*, 178-186.

(46) Bae, J.; Shin, D.; Jeong, H.; Kim, B.-S.; Han, J. W.; Lee, H. Highly water-resistant La-doped Co_3O_4 catalyst for CO oxidation. *ACS Catal.* **2019**, *9*, 10093-10100.

(47) Chen, H.; Wang, Y.; Lv, Y.-K. Catalytic oxidation of NO over MnO_2 with different crystal structures. *Rsc Adv.* **2016**, *6*, 54032-54040.

(48) Zhao, X.; Yang, Q.; Cui, J. XPS study of surface absorbed oxygen of ABO_3 mixed oxides. *J. Rare Earths* **2008**, *26*, 511-514.

(49) Shit, S.; Saha, D.; Saha, D.; Guru Row, T. N.; Rizzoli, C. Azide/thiocyanate incorporated cobalt(III)-Schiff base complexes: Characterizations and catalytic activity in aerobic epoxidation of olefins. *Inorg. Chim. Acta* **2014**, *415*, 103-110.

(50) Varma, S.; Castillo, C. E.; Stoll, T.; Fortage, J.; Blackman, A. G.; Molton, F.; Deronzier, A.; Collomb, M.-N. Efficient photocatalytic hydrogen production in water using a cobalt (III)

tetraaza-macrocyclic catalyst: electrochemical generation of the low-valent Co(I) species and its reactivity toward proton reduction. *Phys. Chem. Chem. Phys.* **2013**, *15*, 17544-17552.

(51) Penninger, M. W.; Kim, C. H.; Thompson, L. T.; Schneider, W. F. DFT analysis of NO oxidation intermediates on undoped and doped $LaCoO_3$ perovskite. *J. Phys. Chem. C* **2015**, *119*, 20488-20494.

(52) Cramer, C. J.; Tolman, W. B.; Theopold, K. H.; Rheingold, A. L. Variable character of O-O and M-O bonding in side-on (η^2) 1: 1 metal complexes of O_2. *Proc. Natl. Acad. Sci. U.S.A.* **2003,** *100*, 3635-3640.

(53) Liu, X.; Hu, J.; Cheng, B.; Qin, H.; Zhao, M.; Yang, C. First-principles study of O_2 adsorption on the $LaFeO_3$(010) surface. *Sens. Actuators, B* **2009**, *139*, 520-526.

(54) Choi, S. O.; Penninger, M.; Kim, C. H.; Schneider, W. F.; Thompson, L. T. Experimental and computational investigation of effect of Sr on NO oxidation and oxygen Exchange for $La_{1-x}Sr_xCoO_3$ perovskite catalysts. *ACS Catal.* **2013**, *3*, 2719-2728.

(55) Saeys, M.; Reyniers, M. F.; Neurock, M.; Marin, G. B. Adsorption of cyclohexadiene, cyclohexene and cyclohexane on Pt(111). *Surf. Sci.* **2006**, *600*, 3121-3134.

(56) Ding, K.; Wang, D.; Yang, P.; Hou, P.; Cheng, X. Enhanced CO catalytic oxidation of flower-like Co_3O_4 composed of small nanoparticles. *RSC adv.* **2016**, *6*, 16208-16214.

(57) Yan, Q.; Li, X.; Zhao, Q.; Chen, G. Shape-controlled fabrication of the porous Co_3O_4 nanoflower clusters for efficient catalytic oxidation of gaseous toluene. *J. Hazard. Mater.* **2012**, *209-210*, 385-391.

(58) Liang, F.; Zhong, W.; Xiang, L.; Mao, L.; Xu, Q.; Kirk, S. R.; Yin, D. Synergistic hydrogen atom transfer with the active role of solvent: Preferred one-step aerobic oxidation of cyclohexane to adipic acid by N-hydroxyphthalimide. *J. Catal.* **2019**, *378*, 256-269.

List of Tables

Table 1. Physical Properties of the Catalysts

Sample	La/Co Atomic Composition (%)			$LaCoO_3$ Content (%)	Crystallite Size (nm)	BET Surface area ($m^2\ g^{-1}$) [a]	Pore diameter (nm) [b]	Pore volume ($cm^3\ g^{-1}$) [c]
	Nominal	EDX	XPS					
La_2O_3	-	-	-	-	40.4	13.1	3.8	0.08
$La_1Co_{0.8}O_3$	1.25	1.36	2.81	77	28.1	6.4	18.6	0.05
$La_1Co_1O_3$	1.00	1.04	1.79	100	21.9	7.1	18.4	0.07
$La_{0.8}Co_1O_3$	0.80	0.72	1.19	80	31.6	4.5	42.0	0.07
Co_3O_4	-	-	-	-	56.0	3.7	48.1	0.04
$La_1Co_1O_3$ -AR [d]	-	-	-	-	20.1	7.8	19.2	0.06

[a] Determined by BET method; [b] Adsorbed volume at P/P0 = 0.995; [c] Determined by BJH method from the desorption branch; [d] catalyst $La_1Co_1O_3$ after reaction.

Table 2. XPS Quantitative Analysis of La_2O_3, $La_1Co_{0.8}O_3$, $La_1Co_1O_3$, $La_{0.8}Co_1O_3$, and Co_3O_4.

Sample	Co^{3+}/Co_{total}	O_β/O_α [a]	Sat_1/Sat_2 [b]	ΔE /eV [c]
La_2O_3	-	3.87	-	-
$La_1Co_{0.8}O_3$	0.47	1.89	1.19	15.12
$La_1Co_1O_3$	0.53	1.41	1.84	14.94
$La_{0.8}Co_1O_3$	0.49	1.34	2.19	15.25
Co_3O_4	0.32	0.91	2.98	15.48

[a] O_β/O_α = ratio of surface adsorbed oxygen to surface lattice oxygen [b] Sat_1/Sat_2 = Co^{2+} to Co^{3+} satellite peak ratios and [c] ΔE = Binding energy difference between the Co $2p_{3/2}$ and the Co $2p_{1/2}$ peaks

Table 3. The Structural Properties of Adsorbed Oxygen and Cyclohexane Molecules.

Sites	Ads Energy (eV)		Bond length (Å)	
	O_2	C_6H_{12}	O-O	C-H
CoO_2(1 1 0)	-0.57	-0.99	1.278	1.113
LaO(1 1 0)	-2.04	-0.82	1.394	0.107
La_2O_3(0 0 1)	-1.82	-0.73	1.314	1.106

Table 4. The Catalytic Performance of Catalysts in Cyclohexane Oxidation [a]

Catalysts	Conversion (%)	K/A ratio	Selectivity (%)			
			Cyclohexanone (K)	Cyclohexanol (A)	K/A oil	By-products [b]
Blank	2.6	1.5	55.7	36.4	92.1	7.9
La_2O_3	2.7	0.6	38.3	60.6	98.9	1.1
$La_1Co_{0.8}O_3$	6.1	2.3	64.2	27.7	91.9	8.1
$La_1Co_1O_3$	8.3	1.8	58.2	31.8	90.0	10.0
$La_{0.8}Co_1O_3$	6.3	1.9	59.6	30.7	90.3	9.7
Co_3O_4	3.9	1.4	54.5	40.1	94.6	5.4

[a] Reaction conditions: cyclohexane, 7.56 ml; reaction time, 1 h; reaction temperature, 423 K; catalyst, 50 mg; K/A, cyclohexanone to cyclohexane ratio; [b] By-products are mainly ring-opened acids such as n-butric, succinic, glutaric, adipic acid and their corresponding esters.

List of Figures

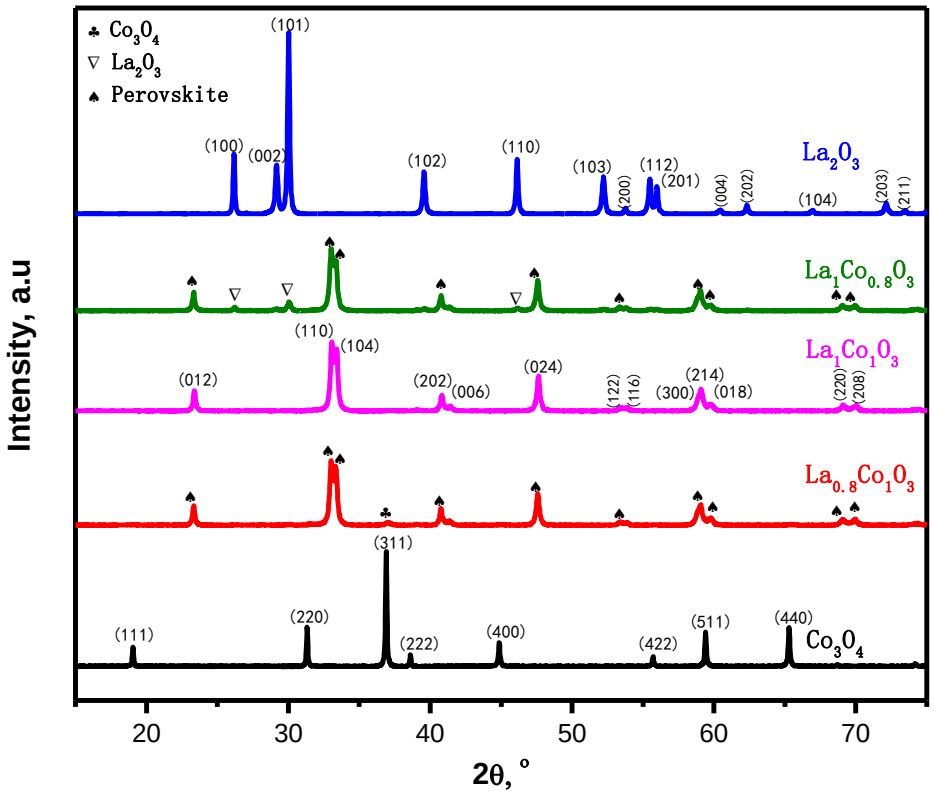

Figure 1. XRD patterns of La_2O_3, $La_1Co_{0.8}O_3$, $La_1Co_1O_3$, $La_{0.8}Co_1O_3$, and Co_3O_4.

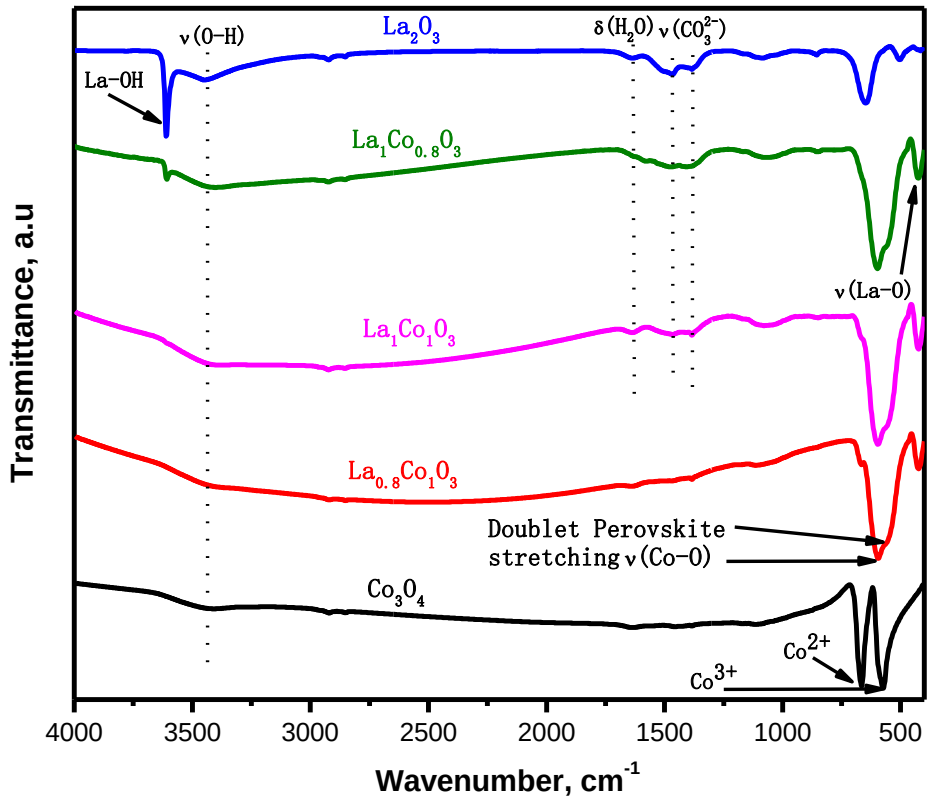

Figure 2. The FTIR spectra of catalysts La_2O_3, $La_1Co_{0.8}O_3$, $La_1Co_1O_3$, $La_{0.8}Co_1O_3$, and Co_3O_4.

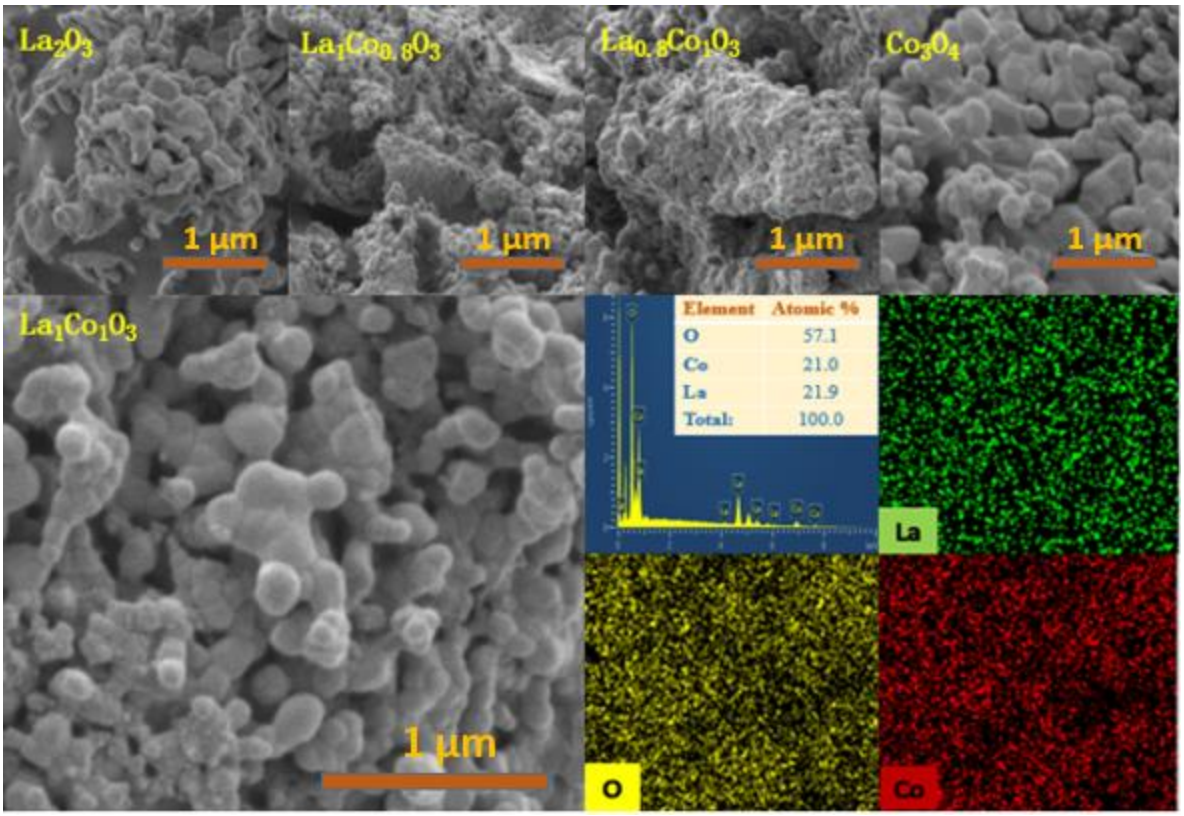

Figure 3. SEM images of La_2O_3, $La_1Co_{0.8}O_3$, $La_1Co_1O_3$, $La_{0.8}Co_1O_3$, and Co_3O_4. Inset: EDX of $La_1Co_1O_3$.

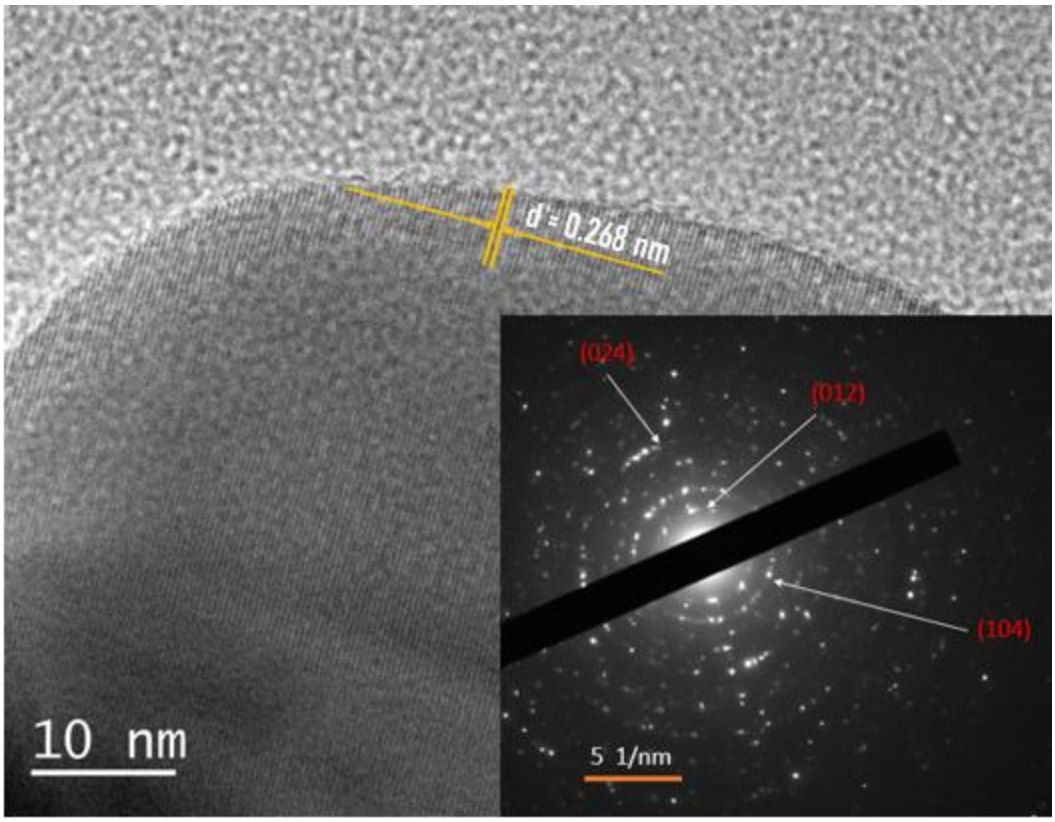

Figure 4. TEM micrographs of $La_1Co_1O_3$ nanoparticle. Inset: Selected area electron diffraction (SAED) pattern.

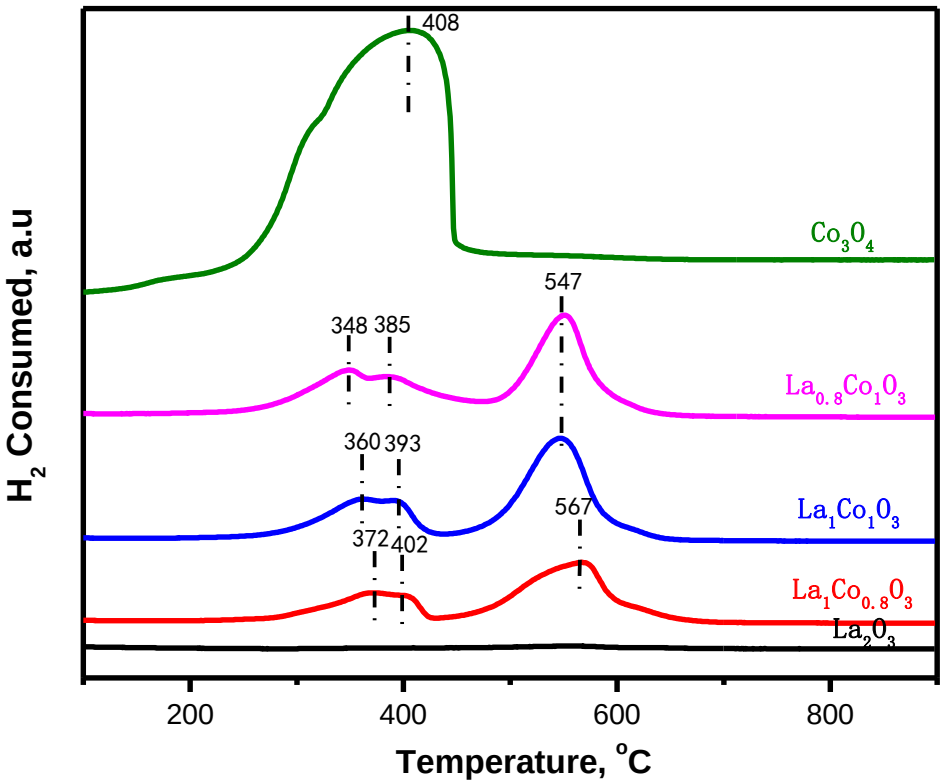

Figure 5. H_2-TPR profiles of catalysts La_2O_3, $La_1Co_{0.8}O_3$, $La_1Co_1O_3$, $La_{0.8}Co_1O_3$, and Co_3O_4.

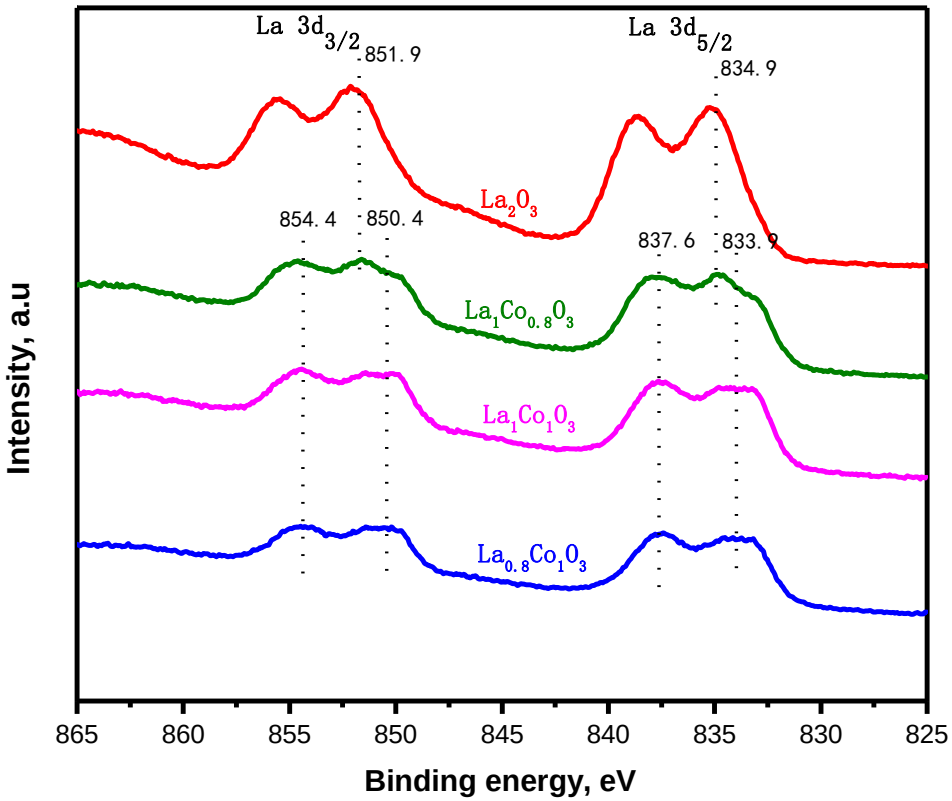

Figure 6. La3d spectra for La_2O_3, $La_1Co_{0.8}O_3$, $La_1Co_1O_3$, $La_{0.8}Co_1O_3$, and Co_3O_4.

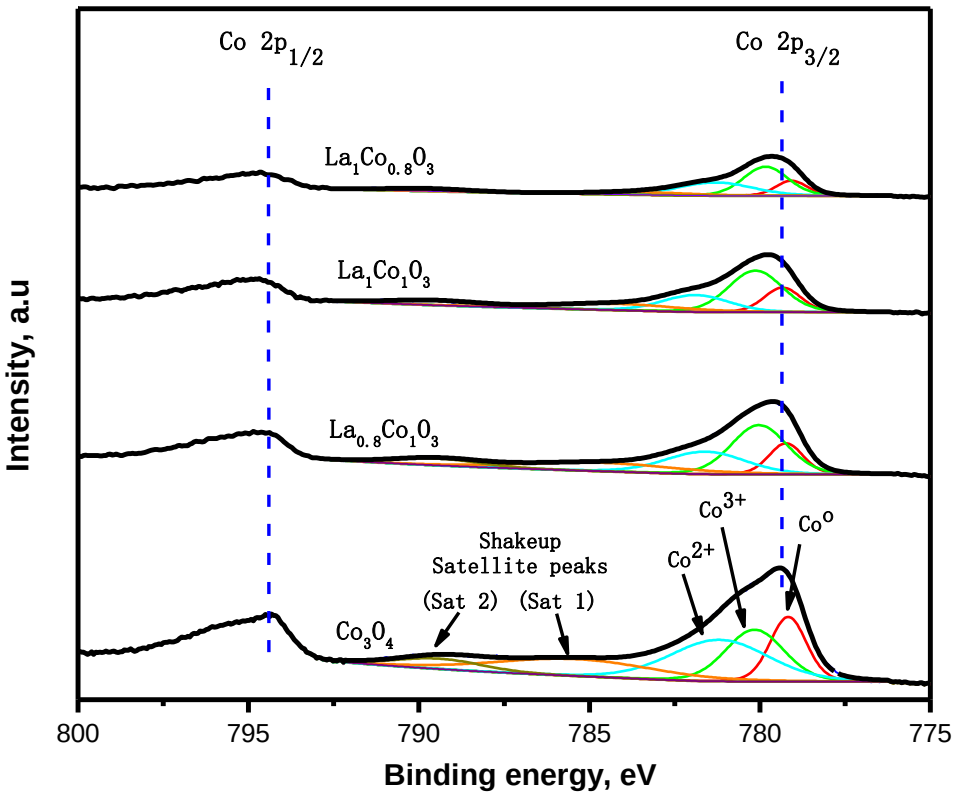

Figure 7. Co 2p spectra for La_2O_3, $La_1Co_{0.8}O_3$, $La_1Co_1O_3$, $La_{0.8}Co_1O_3$, and Co_3O_4.

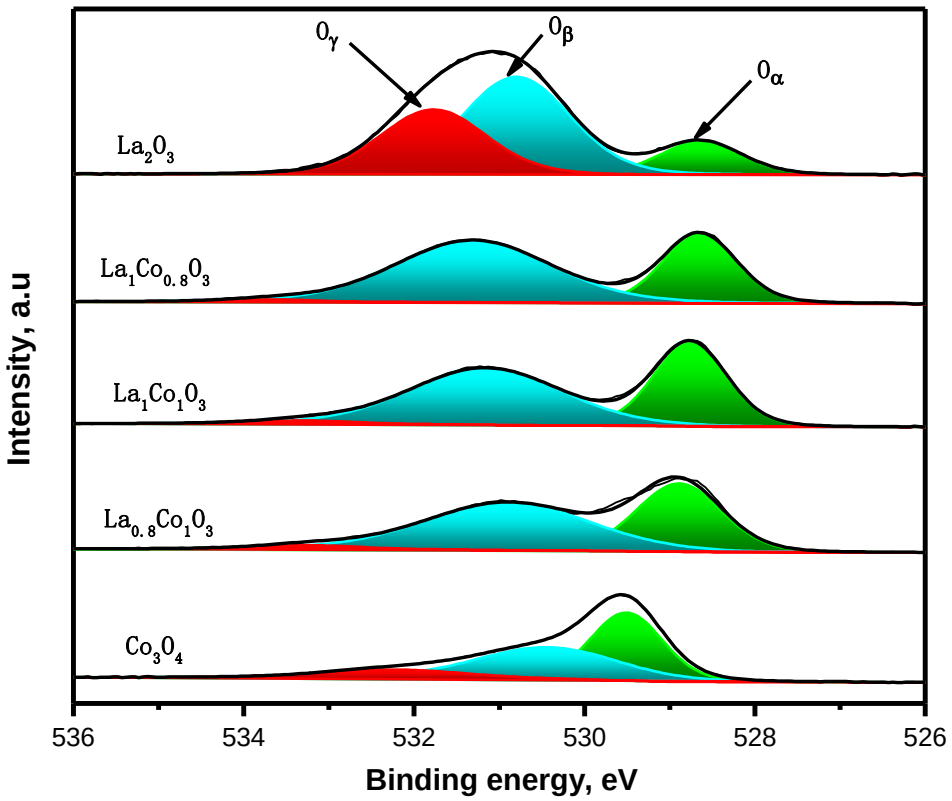

Figure 8. O 1s spectra of catalysts La_2O_3, $La_1Co_{0.8}O_3$, $La_1Co_1O_3$, $La_{0.8}Co_1O_3$, and Co_3O_4.

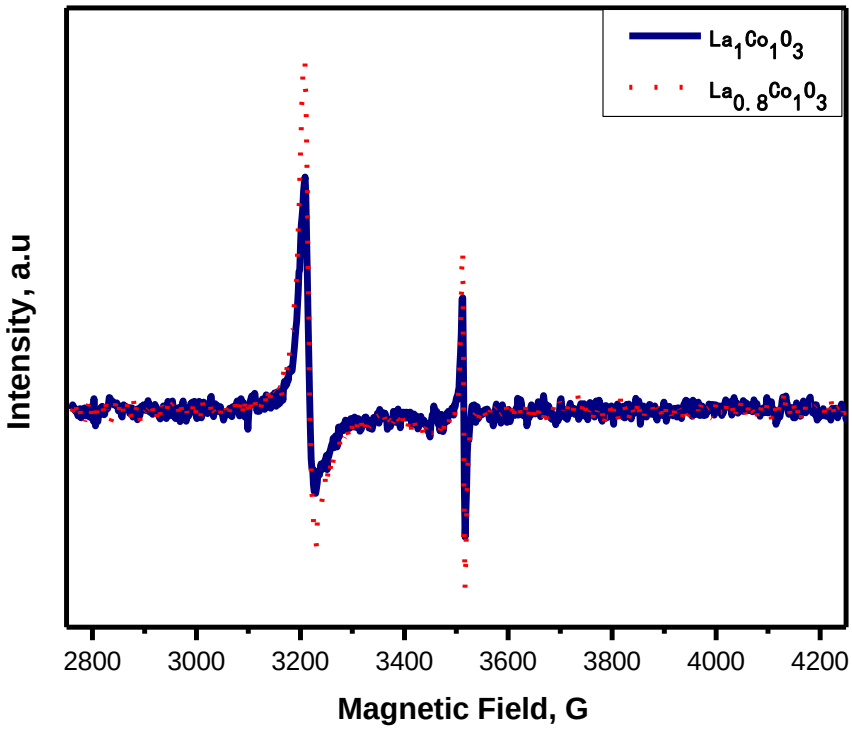

Figure 9. Room temperature EPR spectra for $La_1Co_1O_3$ and $La_{0.8}Co_1O_3$**.**

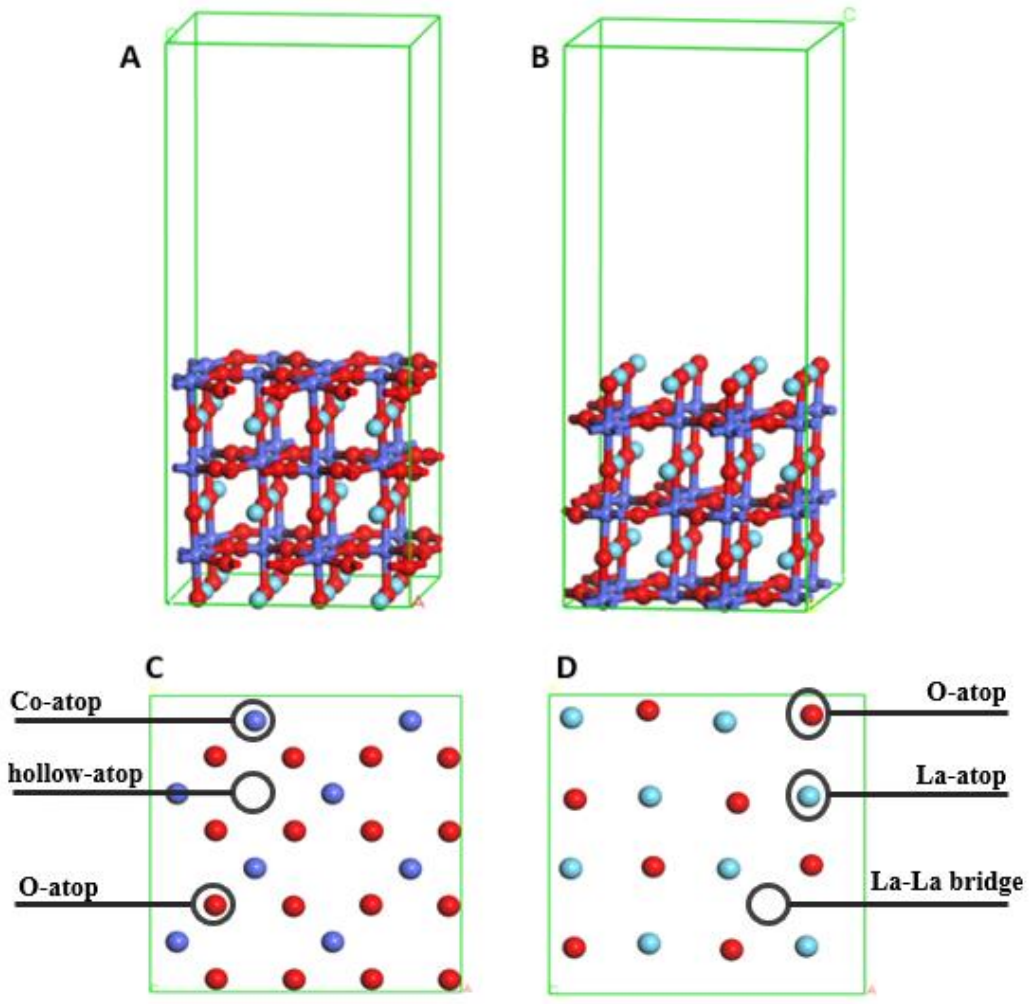

Figure 10. Six-layer slab model of CoO_2(110) (A) and LaO(110) (B) terminations and their unique binding sites as a combination of atop, bridge, and hollow sites (C and D).

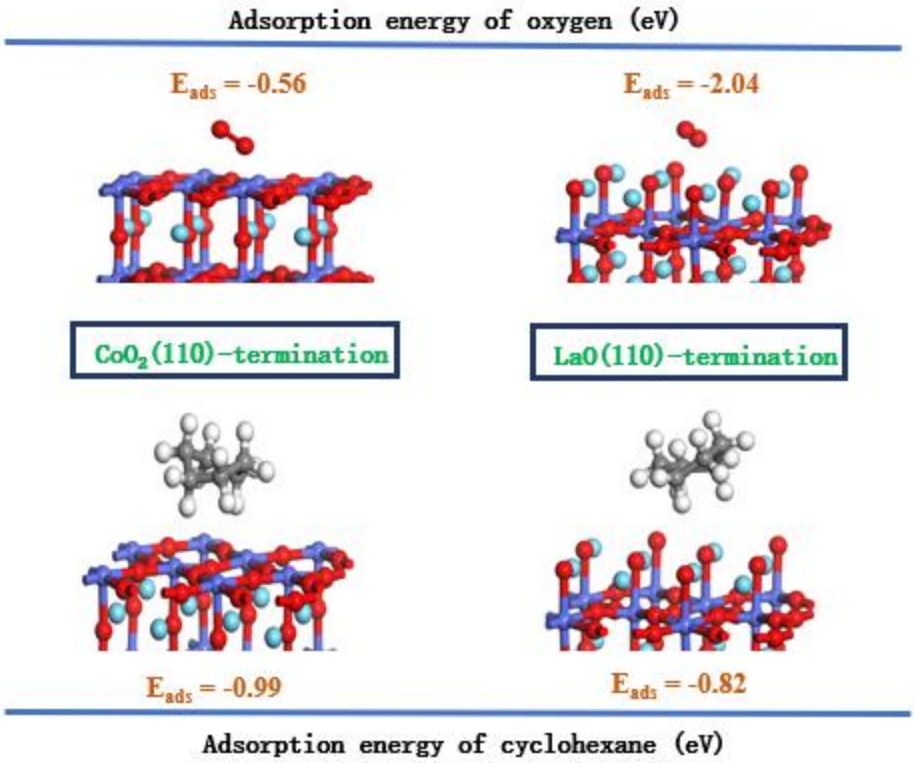

Figure 11. The most stable adsorbate positions of the optimized oxygen and cyclohexane adsorption geometries on the CoO_2(110) and LaO(110) terminations.

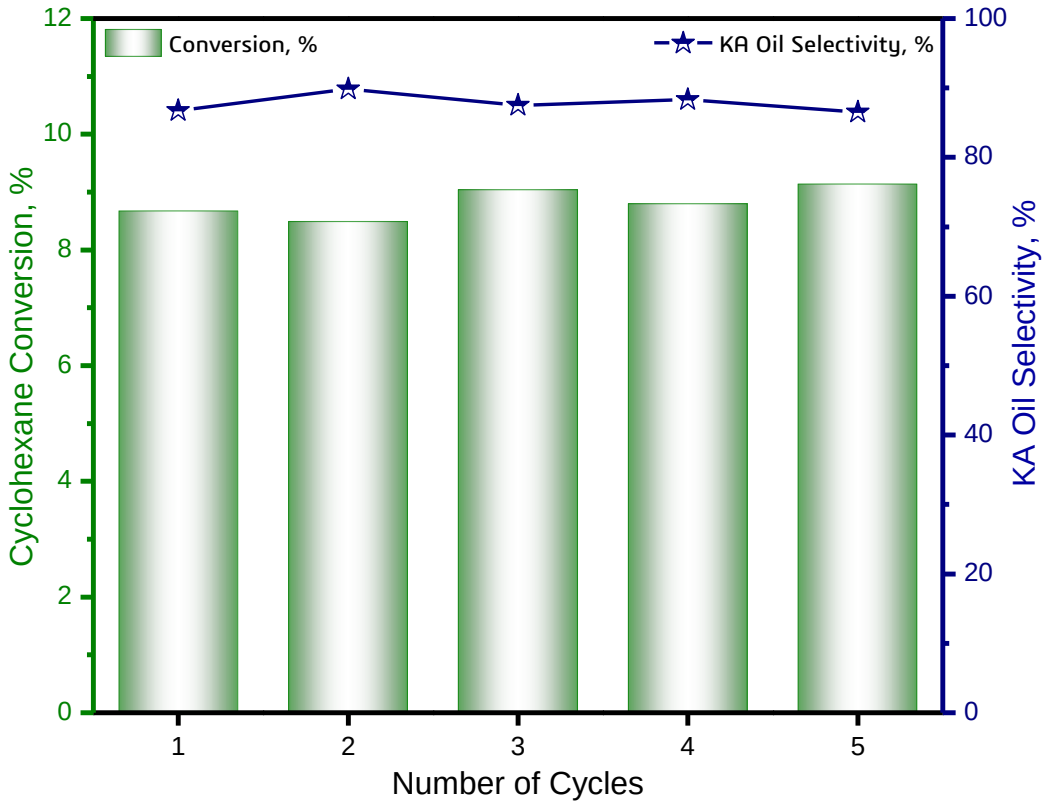

Figure 12. Cyclohexane partial oxidation with recycled $La_1Co_1O_3$ catalyst.

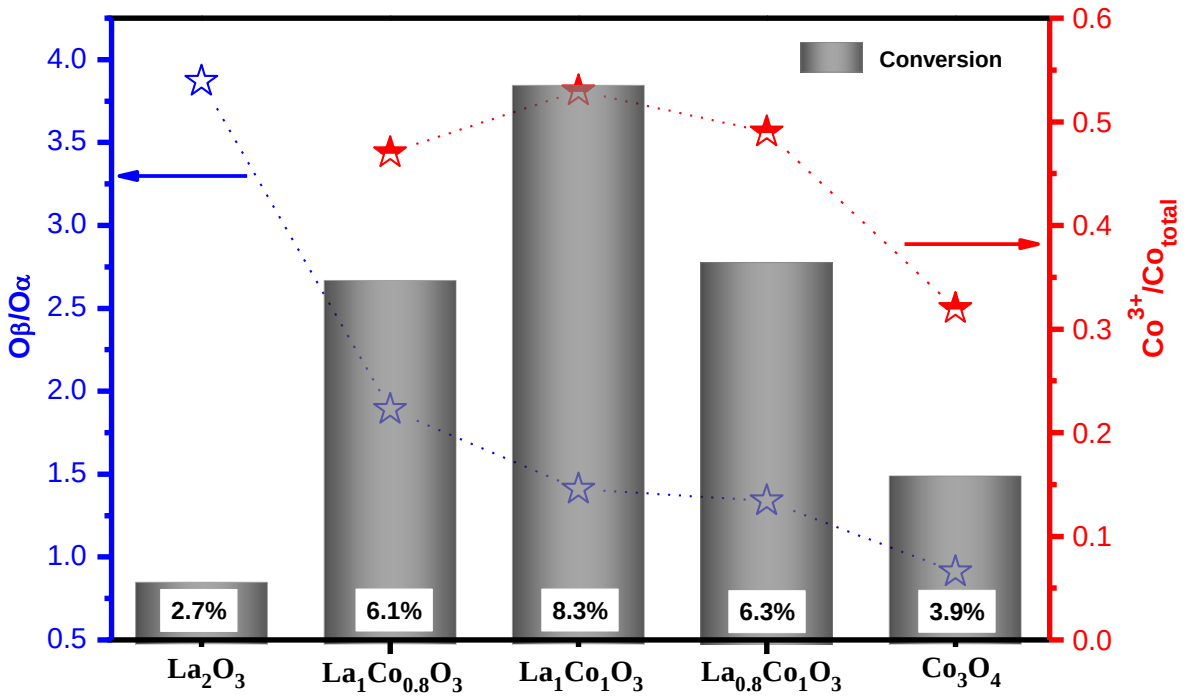

Figure 13. The relationship between Co^{3+}/Co_{total} or O_β/O_α versus the conversion attained by different catalysts.

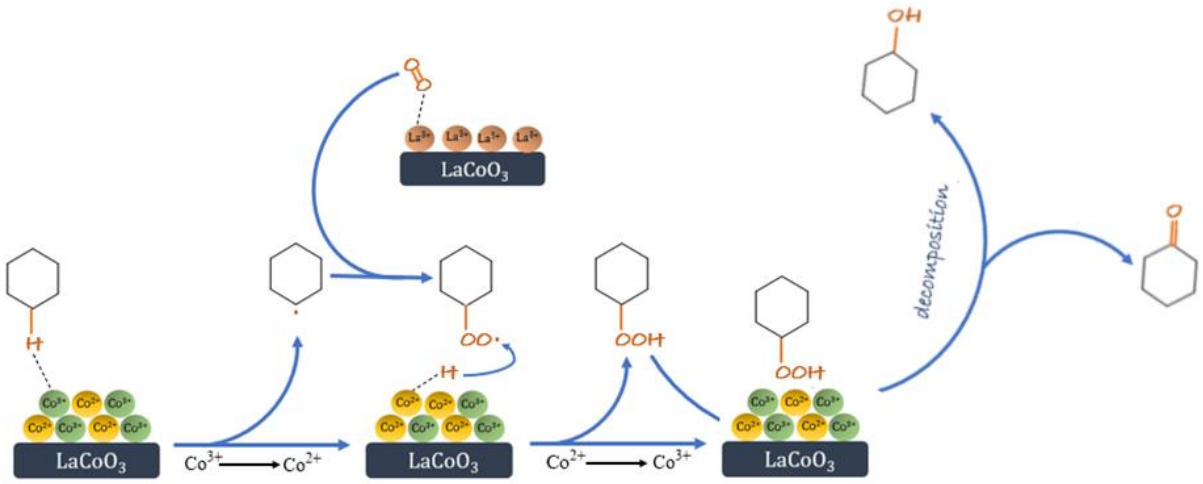

Scheme 1. Reaction mechanism of cyclohexane partial oxidation on $LaCoO_3$

For Table of Content use only